AIAA SciTech Forum
January 3-7, 2022, San Diego, CA & Virtual
AIAA SCITECH 2022 Forum

10.2514/6.2022-2191

Experimental Characterization of Efficiency Modes in a Rotating Magnetic Field Thruster

Tate M. Gill *, Christopher L. Sercel†, Joshua M. Woods‡, and Benjamin A. Jorns§
University of Michigan, Plasmadyamics and Electric Propulsion Laboratory, Ann Arbor, MI, 48109

A comprehensive experimental study of the contributions to overall efficiency of a rotating magnetic field (RMF) thruster is presented. A 5-kW class test article pulsing continuously at 50 Hz and 1% duty cycle is employed for this study. A Faraday probe and a retarding potential analyzer are used to perform spatially-resolved far-field measurements of the beam current and ion energy in the plume. A Langmuir probe and an array of inductive magnetic field probes are applied in the near field to quantify the thermal and magnetic energy of the propellant before acceleration. A set of inductive Pearson coils are used to compare antenna currents in vacuum and plasma-loaded RMF pulses to measure energy coupling to the plasma. These diagnostic measurements are coupled with a phenomenological efficiency model to evaluate the contributors to performance loss including diverging thrust losses, mass utilization efficiency, a polydispersive correction, energy coupling by the RMF, the energy storage modes of the plasma, and the efficiency of conversion of thermal and magnetic energy to directed kinetic energy. The results are compared to measurements of the overall efficiency inferred from direct thrust measurements. It is shown that the energy storage efficiency of the plasma or "plasma efficiency" is the primary loss mechanism for the RMF test article as it corresponds to a loss of approximately 90% of the energy coupled to the plasma. These results are discussed and interpreted in the context of limitations and improvements to RMF Thrusters.

I. Nomenclature

A	=	matrix to convert discretized azimuthal currents to center line magnetic field
A_c	=	cross sectional area of thruster cone
A_{FP}	=	Faraday probe area
A_{wall}	=	thruster interior wall area
α	=	scaling factor
$\mathbf{B}$	=	magnetic field vector
B_z	=	center line axial magnetic field
$\beta(\omega)$	=	frequency dependent B-dot calibration factor
c_{th}	=	neutral gas mean thermal speed
D	=	ambipolar diffusion coefficient
E_B	=	plasma magnetic energy
E_{in}	=	input electrical energy per shot to the RMF
E_{iz}	=	plasma ionization energy
$E_{LC,p}$	=	energy consumed by both LC tanks during plasma shot
$E_{LC,v}$	=	energy consumed by both LC tanks during vacuum shot
E_{mode}	=	energy stored in a given energy mode
$E_{\text{mode,in}}$	=	energy input into a given energy mode
E_p	=	total plasma energy
E_{rad}	=	plasma radiated energy
E_i	=	bulk kinetic energy of ejected ions

*Ph.D. Candidate, Department of Aerospace Engineering, University of Michigan, Ann Arbor, MI. AIAA Student Member
†Ph.D. Candidate, Department of Aerospace Engineering, University of Michigan, Ann Arbor, MI. AIAA Student Member
‡Ph.D. Candidate, Department of Aerospace Engineering, University of Michigan, Ann Arbor, MI. AIAA Student Member
§Assistant Professor, Department of Aerospace Engineering, University of Michigan, Ann Arbor, MI. AIAA Associate Fellow

E_{th}	=	plasma thermal energy
E_{wall}	=	plasma wall losses
e	=	unit charge
ε	=	ion kinetic energy
ϵ_{ex}	=	energy per excitation collision
ϵ_{iz}	=	first ionization energy
η	=	total thrust/impulse efficiency
η_a	=	acceleration efficiency
η_c	=	coupling efficiency
η_d	=	divergence efficiency
η_m	=	mass utilization efficiency
η_p	=	plasma efficiency
η_{pd}	=	polydispersion efficiency
f_{rep}	=	pulse repetition frequency
Γ	=	noise in magnetic field data
$\Gamma(t)$	=	particles per second collected by Faraday probe
I	=	impulse
$I_{DC,p}$	=	current from DC supply during plasma shot
$I_{DC,v}$	=	current from DC supply during vacuum shot
I_{FP}	=	Faraday probe current
$I_{x,p}$	=	current in x antenna during plasma shot
$I_{x,v}$	=	current in x antenna during vacuum shot
$I_{y,p}$	=	current in y antenna during plasma shot
$I_{y,v}$	=	current in y antenna during vacuum shot
j_θ^{post}	=	posterior mean azimuthal current density
j_θ^0	=	prior mean azimuthal current density
j_{FP}	=	Faraday probe measured far-field current density
k_b	=	Boltzmann constant
κ_G	=	probe area correction factor
L	=	thruster length
l_{char}	=	characteristic length for density gradient
M	=	neutral Mass
M_{fill}	=	Steady-state mass present in thruster before pulse
M_{inj}	=	mass injected during one RMF pulse time
M_i	=	ion mass that contributes to thrust
m_i	=	ion atomic mass
$\dot{m}$	=	neutral mass flow rate
μ_0	=	permeability of free space
N	=	number of ions in plume
n	=	plasma number density
n_n	=	neutral number density
ω	=	RMF frequency
P_{in}	=	input electrical power to the RMF
$P_{\text{mode,in}}$	=	input power to a given energy mode
$P_{\text{mode,out}}$	=	power drain from a given energy mode
ϕ	=	plasma potential
Q	=	charge collected by Faraday probe
Q_{axial}	=	component of total slug charge in axial direction
Q_b	=	total slug charge
R	=	radius of probe arm
$R_{LC,x}$	=	real resistance of x coil LC tank
$R_{LC,y}$	=	real resistance of y coil LC tank
r	=	radial coordinate
$\mathbf{r}$	=	observation point for Biot-savart

$\mathbf{r}'$	=	vector from volume element to observation point
Σ_{post}	=	posterior variance for azimuthal current density
Σ^0	=	prior variance for azimuthal current density
$\langle \sigma_{ex} v_e \rangle$	=	excitation reaction rate
T	=	thrust
T_e	=	electron temperature
t_{fill}	=	characteristic steady-state mass fill time
t_{pulse}	=	probe integration time
t_{RMF}	=	RMF pulse on time
Θ	=	characteristic divergence angle of plume
θ	=	polar angle of probe arm relative to thruster center line
u_{ex}	=	effective exhaust velocity of ions
V	=	thruster volume
$V_{BB,p}$	=	voltage of PPU backing bank during plasma shot
$V_{BB,v}$	=	voltage of PPU backing bank during vacuum shot
V_p	=	voltage of B-dot probe
z	=	axial coordinate
Δz	=	width of prior mean current distribution
z_{max}	=	axial location of maximum induced magnetic field

II. Introduction

Inductive pulsed plasma thrusters (IPPTs) offer several potential advantages over mature electric propulsion (EP) architectures such as Hall effect or gridded ion thrusters. Since IPPTs have no inherent dependence on the use of plasma-wetted electrodes, they can operate on non-conventional propellants such as those recovered from in-situ resource utilization or propellants shared by chemical propulsion systems in dual mode architectures [1]. Another benefit of inductive thrusters is that they are commonly operated in a pulsed mode, where the thrust and total power are easily throttled by changing only the pulse repetition rate. This feature enables another form of multi-mode operation where the same system can throttle its thrust while retaining a constant efficiency and specific impulse [2]. Furthermore, since the thrust produced by an inductive thruster is a result of the Lorentz force, the thrust is often a function of the thruster current squared [3]. This scaling indicates that the power output of an IPPT will trend as the fourth power of the thruster size, while the power output of a electrostatic thruster only scales quadratically with thruster size. In light of these advantages, IPPTs are a uniquely attractive emerging high-power electric propulsion concept, and these traits indicate that they are a promising improvement over current state-of-the-art thrusters.

Because inductive thrusters show great potential, there have been multiple efforts to develop and prove this technology in different forms. Arguably, the most successful of these efforts has been the pulsed inductive thruster (PIT). In this architecture, a series of spiral coils induces a plasma current-sheet that accelerates away from the thruster body. The PIT underwent many iterations and extensive testing, and the best performance reported was 7000 s specific impulse at an efficiency of 50% [3–5]. Despite this demonstrated performance and the body of work that exists for PITs, there are still outstanding drawbacks to their implementation. Some key challenges include the high voltages required for efficient operation, 30-60 kV, and difficulty timing the onset and rise of coil currents to match the injected gas.

The rotating magnetic field (RMF) thruster has the potential to overcome key limitations of these previous inductive propulsion concepts. Most notably, since most IPPTs use direct magnetic induction to generate azimuthal plasma currents, their induced plasma currents scale with the magnitude of the coil current. This dependence on coil current amplitude forces the need for high voltages within the power supply which become prohibitive when scaling to high power levels. However, in RMF thrusters, the azimuthal plasma currents are driven through the entrainment of electrons by the rotating field. Induced current therefore becomes a function of the RMF frequency rather than RMF current amplitude. As a direct result, RMF thrusters in principle do not need to access the high level of currents and voltages that historically have been a requirement for efficient IPPT operation [4–6]. Additionally, a reduction in driving circuit stress allows for higher duty cycles in RMF thrusters or could allow for a continuous-wave operation. In this latter mode, plasma currents are constantly driven and produce steady thrust thus avoiding the need to accurately time pulsed currents in the driving coil.

In light of this advantage over other inductive thruster architectures, there have been several efforts to test and characterize RMF devices. Most notably, Magnetic Systems North West and the University of Washington were able to generate the first performance metrics for RMF thrusters. With the Electrodeless Lorentz Force (ELF) thruster, they demonstrated plasmoid ejection and inferred indirectly from time-of-flight and impact pendulum measurements specific impulses from 450 to 6000 s and impulses up to 1.0 mN-s respectively. However, since the body of ELF formed part of the vacuum wall, they were unable to directly measure thrust and specific impulse. Furthermore, because the impact pendulum necessitated the use of a confining magnetic field, ELF was operated in a non-representative environment within their vacuum facility [7, 8]. MSNW later showed with the Electromagnetic Plasmoid Thruster (EMPT) steady operation at 1 kW and high pulse repetition rates at frequencies up to 2800 Hz in a 50 pulse series [9, 10]. Additionally, a group at the Tokyo University of Agriculture and Technology has developed a fully RF discharge thruster and has measured ion ejection speeds of up to 4 km/s [11, 12]. And recently, at the University of Michigan, we have published performance results from our thruster—the PEPL RMFv2—where we demonstrated continuous steady-state operation at 75 pulses per second and powers up to 4.5 kW. These results showed, however, a low per-shot efficiency of at most 0.5% [13].

Our results highlight that, despite recent advances in RMF thruster technology, their performance remains well below other in-family thrusters—most notably PIT—with at most 8% being claimed for a per-shot efficiency [8]. However, it has been claimed that efficiencies of up to 85% are theoretically achievable with an optimum RMF current drive [7]. The reason for this discrepancy in theoretical versus measured performance remains an open question subject to speculation. Weber [8], for example, examined the efficiency breakdown of the ELF thruster and proposed the low efficiency was primarily caused by large radiative losses, which Polzin [5] also noted could be a major driver for PIT. Alternatively, Brackbill et al. [14] suggested through numerical modeling that a low ionization fraction–and by extension mass utilization efficiency—could severely impact ion acceleration and thruster performance. Despite these proposed explanations of low performance, there has yet to be a direct experimental characterization of these losses. Indeed, to date, most test articles have not been operated in a sufficiently representative space environment, and in most cases, only limited diagnostic plume measurements were performed [7–12]. Given our low performance results and the open questions that remain about the physics of these devices, the need is apparent to establish the role of different efficiency modes in the performance of a system operated in a space-like environment. Due to advances that have allowed steady-state continuous pulsed operation for several minutes, this has only recently become possible [13, 15, 16].

The goal of this work is to leverage conventional phenomenological models [17–19] combined with both near and far-field plasma diagnostics to directly measure the contributions of various efficiency losses in a 5-kW class RMF thruster. To this end, this paper is organized in the following way. We begin by reviewing the operational principles for RMF thruster, followed by the derivation of a phenomenological efficiency breakdown. Next, we describe the experimental setup, the test article, and the diagnostic measurements to be taken. Finally, we discuss the results of our measurements and interpret them as they pertain to overall thruster efficiency and performance.

III. RMF Thruster Principles of Operation

We show in Fig. 1 a schematic representation of an RMF thruster which consists of four primary components: a pre-ionization source, steady bias-field electromagnets, multiple primary coil antennas, and a dielectric plasma bounding surface. Fig. 2 illustrates the principle of operation of this system. These devices generate thrust by driving azimuthal current within a plasma slug or plasmoid, which is then accelerated by a Lorentz force interaction with the radial component of both the plasma current self-field and a steady magnetic bias field ($F_{\text{axial}} \propto j_\theta \times B_r$). Here F_{axial} is the thrust force, j_θ is the azimuthal current density, and B_r is the combined radial component of the self and bias magnetic fields. The acceleration process begins with the pre-ionizer delivering a low-ionization-fraction seed plasma into the thruster, which contains a steady diverging bias field with axial and radial components. Then, a set of independently driven RMF antennas are fired in sequence such that they approximate a uniform magnetic field transversely rotating about the axis of the thruster. The frequency of the RMF is selected to be sufficiently higher than the ion gyrotron frequency such that the electrons are selectively magnetized. The newly formed RMF induces axial electron plasma currents and fully ionizes any remaining neutral gas. These axial currents then couple to the radial bias field to generate torque on the electrons, which drives an azimuthal electron current in the opposite direction to the RMF. A single pulse concludes with these azimuthal currents pushing off both the radial bias field as well as the radial self-field to accelerate the electrons, which carry with them the heavier ions via ambipolar electric fields. These pulses can then be carried out repeatedly at some pulse repetition rate to deliver continuous steady-state thrust. However, since the physics of single pulse are independent of pulse rate, in principle an RMF thruster can be throttled across a wide range wile maintaining a constant efficiency.

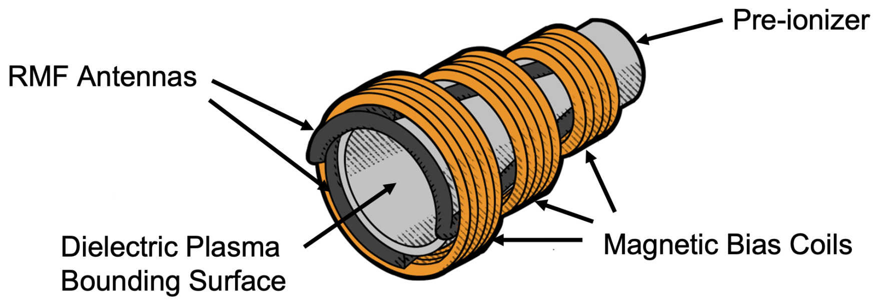

Fig. 1 Primary RMF thruster components

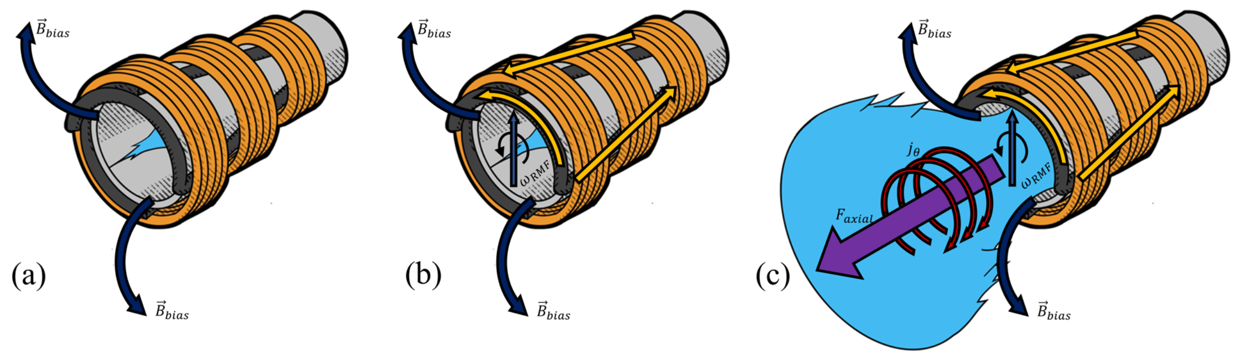

Fig. 2 Illustrative representation of RMF thruster operation. (a) Seed plasma injected into the thruster body. (b) Antennas fire in sequence and approximate a uniform transversely rotating magnetic field which magnetizes the electrons. (c) RMF continues to ionize neutrals, and induced azimuthal electron current accelerates via the Lorentz force.

IV. Phenomenological Efficiency Model

In this section, we derive terms for the different phenomenological efficiency modes for an RMF thruster. Typically, for electric propulsion devices that operate at steady state, the efficiency is written as the ratio of jet power to input electrical power:

$$\eta = \frac{T^2}{2\dot{m}P_{in}}, \tag{1}$$

where T is the thrust, $\dot{m}$ is the mass flow rate of propellant, and P_{in} is the input electrical power. For pulsed thrusters, instead of with steady-state quantities, we are interested in per-shot properties. We therefore instead adopt an efficiency based on total impulse. This is as written as

$$\eta = \frac{I^2}{2ME_{in}}, \tag{2}$$

where I is the impulse, M is the available propellant mass, and E_{in} is the input electrical energy. For RMF thrusters in particular, we seek a phenomenological breakdown of the total efficiency in discrete terms with physical significance. These terms are meant to explain the various loss mechanisms inherent to these devices and provide a basis for the optimization of their operation.

We start by defining impulse as

$$I = M_i\, u_{ex} \cos\Theta, \tag{3}$$

where M_i is the ion mass that contributes to thrust, u_{ex} is the effective ion exhaust velocity, and Θ is the effective divergence angle of the exhaust plume. This angle represents the contribution of momentum directed in the axial direction—which is useful for thrust—versus total momentum. It is approximated as

$$\Theta = \cos^{-1}\left(\frac{Q_{axial}}{Q_b}\right) \tag{4}$$

where Q_{axial} is the component of emitted charge in the axial direction and Q_b is the total charge emitted in the beam. We next approximate the effective exhaust velocity u_{ex} as the mean exit velocity of the ions:

$$u_{ex} = \int f(\varepsilon)\sqrt{\frac{2\varepsilon}{m_i}}d\varepsilon, \tag{5}$$

where, $f(\varepsilon)$ is the ion energy distribution function, ε is the ion energy, and m_i is the mass of a single ion. Substituting the relation above into Eq. 3 and then into the right side of Eq. 2 yields

$$\eta = \frac{1}{2ME_{in}}\left(\cos\Theta M_i \int f(\varepsilon)\sqrt{\frac{2\varepsilon}{m_i}}d\varepsilon\right)^2 \tag{6}$$

$$= \frac{NM_i\cos^2\Theta}{ME_{in}}\left(\int f(\varepsilon)\sqrt{\varepsilon}d\varepsilon\right)^2, \tag{7}$$

where N is the number of ions, from the definition $M_i/m_i = N$. We now multiply and divide by average ion energy, $\langle\varepsilon\rangle = \int f(\varepsilon)\varepsilon d\varepsilon$, to find

$$\eta = \cos^2\Theta\frac{M_i}{M}\frac{\left(\int f(\varepsilon)\sqrt{\varepsilon}d\varepsilon\right)^2}{\langle\varepsilon\rangle}\frac{N\langle\varepsilon\rangle}{E_{in}}, \tag{8}$$

where we can simplify by defining the kinetic ion energy in the plume as $E_i = N\langle\varepsilon\rangle$. This yields

$$\eta = \left(\cos^2\Theta\right)\left(\frac{M_i}{M}\right)\left(\frac{\left(\int f(\varepsilon)\sqrt{\varepsilon}d\varepsilon\right)^2}{\langle\varepsilon\rangle}\right)\left(\frac{E_i}{E_{in}}\right). \tag{9}$$

Armed with this result, we now can introduce key efficiency terms for the system. The first is the divergence efficiency, η_d, which is defined from Eq. 9 as

$$\eta_d = \cos^2\Theta. \tag{10}$$

Physically, this result shows that as divergence angle increases, efficiency decreases. This is intuitive since the momentum flux of ions in the radial direction symmetrically cancels out and therefore does not contribute to net thrust. We next define a mass utilization efficiency

$$\eta_m = \frac{M_i}{M} = \frac{M_i}{M_{fill} + M_{inj}}. \tag{11}$$

This represents physically the specific impulse loss due to incomplete ionization where any remaining neutrals are not accelerated.

Here we have expressed the total mass per shot as the summation of two constituent parts, $M = M_{fill} + M_{inj}$, where M_{fill} is defined at the mass accumulated inside the thruster before the start of the RMF discharge and M_{inj} is the mass injected into the thruster during the RMF pulse. Since we are only looking at the per-pulse efficiency, it is important to note we do not take into consideration the contribution of any propellant injected in the dead-time between pulses as it is not "available" to the RMF. If we were to look at the steady state performance, this additional propellant flow would contribute an additional loss term proportional to the duty cycle of the thruster.

As a next step, we define the polydispersive efficiency:

$$\eta_{pd} = \left(\frac{\left(\int f(\varepsilon)\sqrt{\varepsilon} d\varepsilon \right)^2}{\langle \varepsilon \rangle} \right). \tag{12}$$

Physically this is not a direct energy loss but rather stems from our definition of impulse which is related to the root mean square of ion energy versus plume kinetic energy which is instead proportional to the mean ion energy. This term becomes important when there is a wide range of ion energies and is unity for a mono-energetic beam. With these definitions for efficiency, Eq. 9 reduces to

$$\eta = \eta_d \eta_m \eta_{pd} \frac{E_i}{E_{in}}. \tag{13}$$

We next introduce a new term for plasma energy that represents the sum of the channels in which the plasma can store or release energy:

$$E_p = E_B + E_{th} + E_{iz} + E_{rad} + E_{wall} + ..., \tag{14}$$

where E_B denotes the magnetic energy stored in the azimuthal currents induced by the RMF, E_{th} is the thermal energy stemming from any heating of the plasma by the driven currents, E_{iz} is the ionization energy associated with converting the incoming gas to plasma, E_{rad} electromagnetic radiation energy that stems from radiation of the excited ions and neutrals, and E_{wall} is the energy lost due to plasma recombining at the walls. The terms in Eq. 14 are not an exhaustive list but represent the primary energy loss and storage channels available to the plasma. With this definition, we now introduce a plasma coupling efficiency term

$$\eta_c = \frac{E_p}{E_{in}}. \tag{15}$$

This coupling efficiency is a representation of the fraction of the energy put into the RMF antenna circuits is transferred to the plasma slug. It allows for the fact that some power may be restively dissipated either in the antenna circuit or coupled into other structures. This efficiency term can be directly measured by comparing the ring-down of the RMF current in vacuum versus the ring-down in plasma [13]. Armed with this result, we now can re-write Eq. 13 as

$$\eta = \eta_d \eta_m \eta_{pd} \eta_c \frac{E_i}{E_p}. \tag{16}$$

We then multiply the above expression by $(E_B + E_{th})/(E_B + E_{th})$ to form

$$\eta = \eta_d \eta_m \eta_{pd} \eta_c \frac{E_B + E_{th}}{E_p} \frac{E_i}{E_B + E_{th}}. \tag{17}$$

This lends itself to two additional efficiency terms:

$$\eta_p = \frac{E_B + E_{th}}{E_p} \tag{18}$$

and

$$\eta_a = \frac{E_i}{E_B + E_{th}}. \tag{19}$$

η_p represents a plasma efficiency, or how much energy is lost in the plasma formation process possibly to radiation, ionization, or the thruster walls and is unrecoverable as kinetic energy downstream. η_a in Eq. 19 is an acceleration efficiency, which is a measure of how effective the conversion is between potential thermal and magnetic energy in the plasma to directed kinetic energy. With these last two terms, the final phenomenological efficiency breakdown can be written as

$$\eta = \eta_d \eta_m \eta_{pd} \eta_c \eta_p \eta_a. \tag{20}$$

With this result, we have a model for the various contributions to the efficiency of the RMF thruster. In the next section, we turn to describing an experimental setup for characterizing these efficiency modes.

V. Experimental Setup

In this section, we describe the experimental setup for this work. This includes overviews of the test article, test facility, diagnostics, and data acquisition techniques.

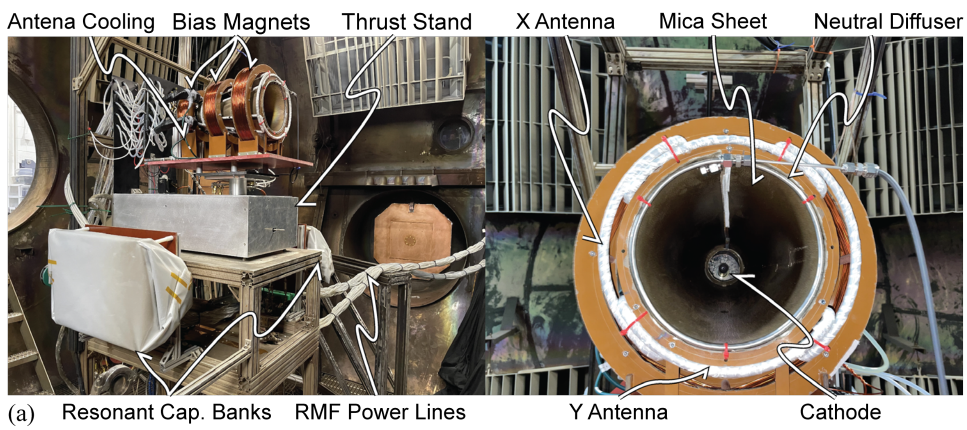

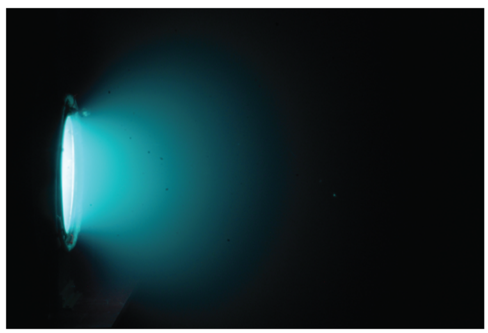

(b)

Fig. 3 (a) Diagram illustrating thruster components (b) 10 second exposure of PEPL RMFv2 thruster firing at 4.0 mg/s Xe and 2.0 kA RMF peak currents

A. Test Article and Power Supply

We show in Fig. 3 our test article, the PEPL RMFv2, inside the vacuum facility at the University of Michigan. This figure also shows a 10 second exposure photograph of the thruster firing at one operating condition interrogated for this work. Our RMF test article is constructed from five major components. A 20 A LaB6 hollow cathode acts as the pre-ionization source, which discharges to an annular steel anode and provides a constant 1.3 mg/s Xe flow. Next, we have three bias-field electromagnets that are constructed around a dielectric G10 structure to minimize coupling losses [20]. Situated inside the bias magnets are the two RMF antennas, each of which consists of a centrally water-cooled copper tube bent to form a single-turn Helmholtz pair. The RMF antennas are oriented orthogonal to each other and referred to as the "x" and "y" antennas depending on their direction, horizontal and vertical respectively. Each antenna is connected in series to a resonant capacitor bank forming an oscillating LC tank circuit. The tank circuits receive power from the RMF power processing unit (PPU), which is situated outside of the chamber. The RMF PPU drives each tank circuit at its resonant frequency with a voltage square-wave and is therefore able to generate kiloamp level currents needed through the RMF antenna. A schematic of the RMF PPU is shown in Fig. 4. Further radially inside the RMF antenna is a mica cone that acts as the plasma bounding surface. Lastly, an annular neutral diffuser is situated at the exit plane of the thruster and injects the remaining neutral propellant upstream. Additional details on the PEPL RMFv2 test article are provided in Sercel et al. [13].

We operated the RMF thruster test article with three different neutral mass flow rates while probe data was collected. These operation conditions are listed in Table 1 and correspond to a range around the local efficiency maximum seen in previous RMF thruster testing [13]. Figure 3(b) shows the PEPL RMFv2 operating at the 4.0 mg/s Xe flow condition.

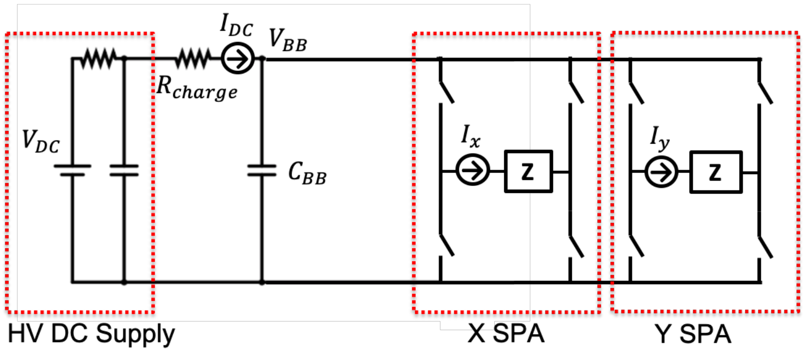

Fig. 4 Schematic of RMF PPU showing the DC supply current I_{DC}, backing capacitor bank C_{BB}, and the two switching pulse amplifiers (SPAs) which drive the LC impedance (Z) of the x and y antennas respectively.

Table 1 RMF Thruster Operating Conditions

Operating Parameter	Value		
Total Flow Rate [mg/s Xe]	2.7	4.0	5.4
Cathode Flow Rate [mg/s Xe]	1.3		
Peak Bias Magnetic Field [G]	120		
RMF Magnitude [kA pk-pk]	2.0		
Pulse Repetition Rate [Hz]	50		
RMF Duration [μs]	200		
RMF Frequency [kHz]	400		

B. Test Facility and Measurement Locations

The experimental campaign was conducted in the Large Vacuum Test Facility (LVTF) at the University of Michigan. This vacuum facility measures 6 m in diameter by 9 m long and can pump a maximum of 600 kL/s of xenon [21]. The pressure inside the vacuum facility was monitored by a Stabil ion gauge aligned with the thruster exit plane and located 1 m radially distance from the thruster body. Background pressure during testing was on the order of 2×10^{-6} Torr N_2. Fig. 5 shows a schematic of the RMF thruster and associated diagnostics in LVTF.

In the thruster far-field, we made measurements using a Faraday probe (FP) and a retarding potential analyzer (RPA) which are housed on polar probe arm. The probe head was located 1.5 m from the thruster exit plane and was swept about a polar angle (as viewed from above). Data for the FP was collected in 5° increments from 0° to 180°, and data from the RPA was taken along thruster center-line. Our near-field probe suite consisted of an single Langmuir probe (LP) situated in the thruster exit plane at half the thruster exit radius and an array of four inductive B-dot probes placed along thruster center line with 8.3 cm axial spacing. The currents to the two RMF antenna were measured using Pearson coils and compared between vacuum and plasma-loaded shots. We monitored the thruster operation with a high-speed camera focused transversely across the thruster exit plane that was capturing at 50,000 frames per second.

C. Diagnostics

The probes which we employed for this experiment are shown in Fig. 6. The FP consisted of a 1.74 cm diameter molybdenum ion collector surrounded by an 0.54 cm thick annular guard ring with a 0.05 cm gap between guard and collector. Both the guard ring and ion collector were biased to ion saturation at -28.6 V relative to facility ground. The RPA used has a 2.32 cm^2 aperture, four internal grids, and an ion collector. The RPA's grids in order as seen by the plasma are a floating plasma attenuation grid, a primary electron suppression grid, a ion selection grid, and lastly a secondary electron suppression grid. During this experiment, the two electron suppression grids were biased to -50 V, the ion collector was biased to -9 V, and the ion selection grid was swept from 0 to 200 V all relative to ground. The near-field LP consisted of a 0.127 mm diameter by 1.270 mm long tungsten wire oriented along the flow direction and was biased from -100 to +50 V. Currents from the FP, LP, and RPA passed through 1.5 kOhm, 1.5 kOhm, and 90 kOhm

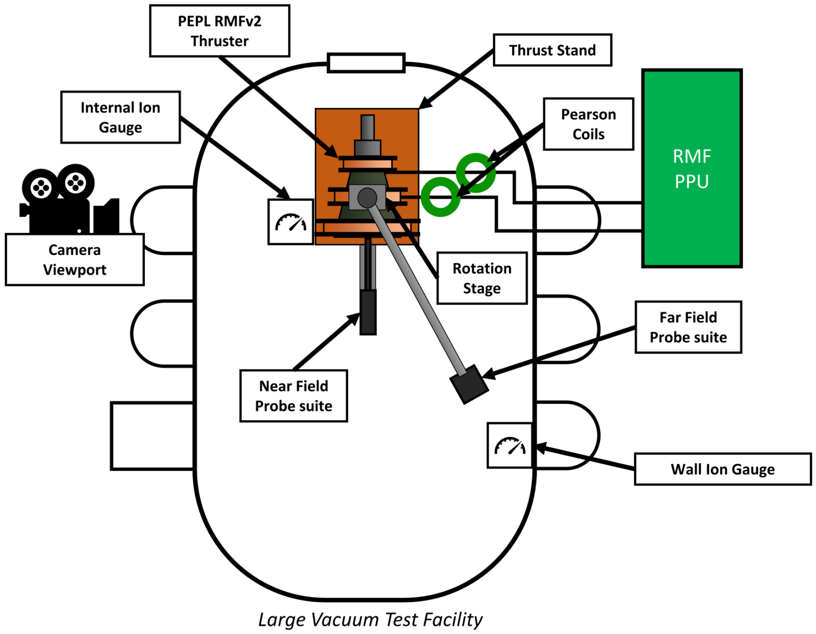

Fig. 5 Schematic of experimental setup inside the Large Vacuum Test Facility

current shunts respectively and were recorded with a 16 bit digital oscilloscope capturing at 1 MS/s. The B-dot probes in the near-field were constructed of roughly 100 turns of copper wire wrapped around a 7.5 mm diameter G10 rod, and have an approximate sensitivity of 10^4 T/Vs. Each of the four B-dot probes was calibrated in accordance with best practices [22] from 1 to 500 kHz. The two Pearson coils were placed around the power lines for the RMF and have a sensitivity of 0.1 V/A. The output of the coils was then fed into 100:1 compensated oscilloscope probes.

D. Data acquisition

To generate time-resolved data from our probe measurements, we acquired data from 500 plasma shots and binned each current trace into 12 μs sections. The integrated charge for each bin is then averaged across shots and compiled into time-resolved measurements across conditions, such as the bias voltage for the RPA and LP, or the angle for the FP. As an example, for RPA measurements, we started with a series of 500 ion collector current traces for each ion selection grid voltage. Then, for each current trace we calculated the charge collected during each 12 μs slice, and averaged for all 500 bins at the same time and voltage. We then arranged the average quantities in chronological order and as a function of voltage to create a contour plot of signal intensity as function of both time and grid voltage such as is shown in Fig. 11. For this technique to work, it was necessary to align each signal trace relative to a common reference. For this purpose each probe acquisition was triggered from the command signal to the RMF PPU such that the probe currents acquired were all relative to the start of the RMF pulse. We show in Fig. 7, reference waveforms for the RMF current, FP, and RPA to demonstrate this alignment method.

VI. Probe Analysis

In this section, we demonstrate how the probe measurements were used to calculate the efficiency terms in section IV.

A. Divergence Efficiency

From Eq. 4 and Eq. 10, we can measure divergence efficiency as

$$\eta_d = \left(\frac{Q_{axial}}{Q_b}\right)^2, \tag{21}$$

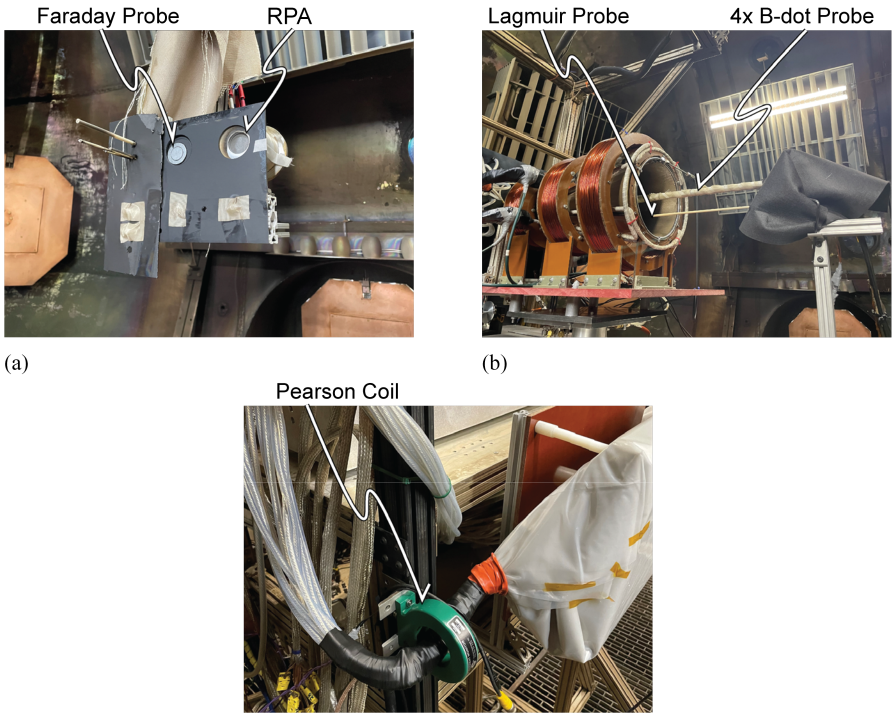

(a) (b) (c)

Fig. 6 Images of the a) far-field probes, FP and RPA, b) near-field probes B-dot probes and LP, and c) Pearson coil used in this experimental campaign.

where again Q_b is the total beam charge emitted over an RMF pulse, and Q_{axial} is the axial component of that charge. If we integrate the collected FP current over a pulse and the forward-facing hemisphere we can compute these two terms as the following:

$$Q_b = 2\pi R^2 \int_0^{\pi/2} \frac{Q(\theta, R)}{A_{FP} + \kappa_G} \sin(\theta) d\theta, \tag{22}$$

where R is the radius of the FP probe, A_{FP} is the probe area and κ_G is a correction factor as presented by Brown et al. [23], and Q is the charge collected by the FP and is defined as

$$Q(\theta, R) = \int_0^{t_{pulse}} I_{FP}(\theta, R) dt, \tag{23}$$

where $I_{FP}(\theta, R)$ is the current collected by the FP as a function of the polar angle about the thruster and the radial distance to the probe R, and t_{pulse} is the integration time to collect all the ejected ions. Note, t_{pulse} is a constant for all the integrated probe measurements and is equal to $1\,ms$. Q_{axial} is similarly given by

$$Q_{axial} = 2\pi R^2 \int_0^{\pi/2} \frac{Q(\theta, R)}{A_{FP} + \kappa_G} \sin(\theta)\cos(\theta) d\theta \tag{24}$$

where the extra $\cos(\theta)$ term accounts for the axial component of the probe current.

B. Mass Utilization Efficiency

The mass utilization term also comes from the FP measurements in addition to an assumption of the neutral mass distribution. The injected neutral mass M_{inj} during the shot is found by multiplying pulse time t_{pulse} by the constant mass flow rate from the mass flow controller. For the sake of consistency, we use the integration time $t_{pulse} = 1\,ms$

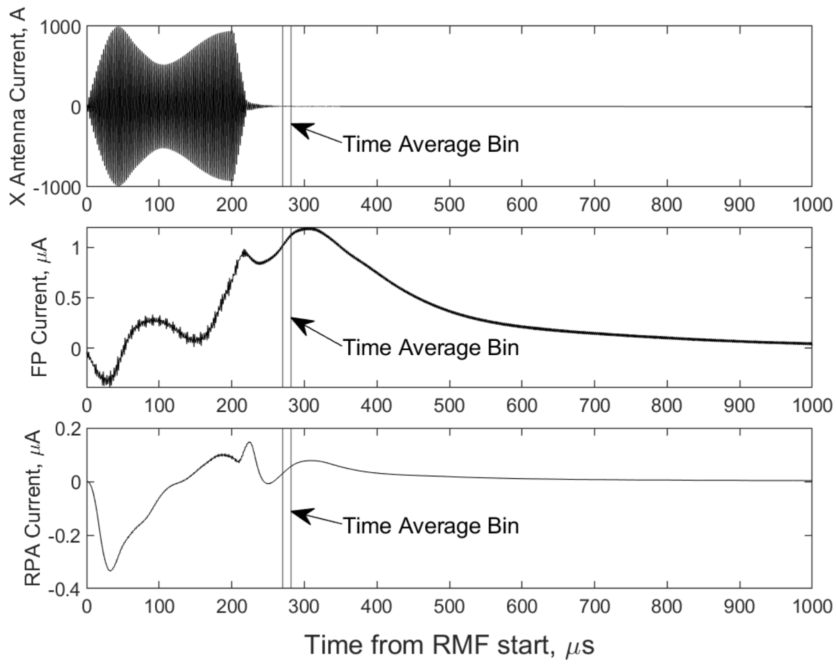

Fig. 7 RMF current waveform, Faraday probe trace, and RPA probe trace aligned in time with a representative 12 μs time-bin shown. Data taken from 5.4 mg/s Xe flow condition, FP at $90°$, and RPA at 60 V ion selection bias.

instead of the shorter RMF discharge duration $t_{RMF} = 200\,\mu s$. Futhermore, the filled neutral mass M_{fill} is found by assuming a steady-state thermal diffusion in the thruster cone where the mass density is given as

$$\rho = \frac{4\dot{m}}{A_c c_{th}}, \tag{25}$$

here A_c is the cross-sectional area of the thruster, and c_{th} is the mean thermal speed of the neutral gas which we assume to be at room temperature; explicitly 218 m/s. Using this assumption and integrating over the thruster volume M_{fill} reduces to

$$M_{fill} = \frac{4\dot{m}L}{c_{th}}, \tag{26}$$

where L is the length of the thruster cone. We found for our thruster geometry and flow rates that M_{fill} is 5.6 times larger than M_{inj}, and M_{fill} is on the order of 2×10^{-8} kg. The ion mass from the FP is given by

$$M_i = \frac{m_i}{e} Q_b, \tag{27}$$

where m_i is the ion mass and Q_b is the total beam charge from Eq. 22. Note, for Eq. 27 we made the assumption that all the ions are singly charged. With these three terms, we can evaluate the mass utilization efficiency using Eq. 11.

C. Coupling Efficiency

As previously mentioned in section IV, the coupling efficiency can be calculated by comparing the current waveforms of the RMF antenna between plasma-loaded and vacuum shots. In Fig. 8 we show representative waveforms for both plasma-loaded and vacuum RMF pulses, and again Fig. 4 is a schematic of the RMF PPU with the relevant currents and voltages labeled. Coupling efficiency as defined in Eq. 15 is also equivalent to

$$\eta_c = 1 - \frac{E_{LC,p}}{E_{LC,p} + E_p}, \tag{28}$$

where $E_{LC,p}$ is the energy consumed by the oscillating LC tank of the PPU during a plasma-loaded shot. $E_{LC,p}$ and E_p are the total of the input electrical energy to the system and are measured by

$$E_{in} = E_p + E_{LC,p} = \frac{V_{BB,p} I_{DC,p}}{f_{rep}}, \tag{29}$$

where V_{BB} is the average voltage of the backing capacitor bank, I_{DC} is the current from the high voltage power supply, f_{rep} is the pulse repetition rate, and the subscript $_p$ denotes values for a plasma-loaded shot.

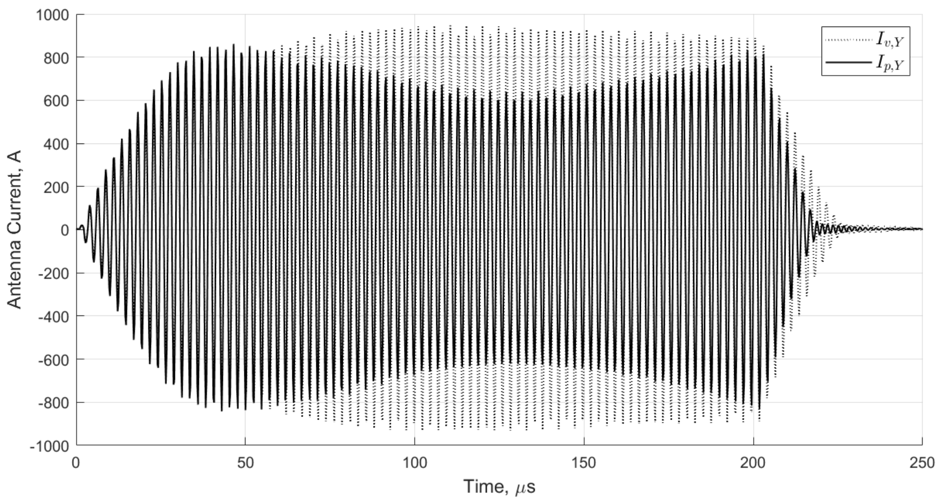

Fig. 8 Current waveforms in the Y antenna for both plasma-loaded and vacuum conditions. Plasma loaded case corresponds to the 4.0 mg/s condition in Table 1.

We can break off the energy consumption from the LC tank as

$$E_{LC,p} = R_{LC,x} \int_0^{t_{pulse}} I_{x,p}^2 dt + R_{LC,y} \int_0^{t_{pulse}} I_{y,p}^2 dt, \tag{30}$$

where $R_{LC,x}$ and $R_{LC,y}$ are the constant resistances of the LC tanks during the RMF pulse, and I_x and I_y are the currents in the antennas for the x and y circuits respectively. We can replace $R_{LC,x}$ and $R_{LC,y}$ in the above equation by using the energy consumed in a vacuum shot. For a vacuum shot, there is no plasma loading and the energy consumed by both the LC tanks is

$$E_{LC,v} = \frac{V_{BB,v} I_{DC,v}}{f_{rep}}, \tag{31}$$

where the subscript $_v$ denotes values for a vacuum shot. The resistance of each LC tank can now be approximated as

$$R_{LC,x/y} = \frac{\frac{1}{2} E_{LC,v}}{\int_0^{t_{pulse}} I_{x/y,v}^2 dt}, \tag{32}$$

where the subscript $_{x/y}$ denotes either the x or y antenna values. The constant 1/2 in Eq. 32 above corresponds to an assumption that the two antenna circuits are close in resistance and they each consume half the total energy consumed by the LC tanks. Namely, the assumption can be stated as

$$\frac{|R_{LC,x} - R_{LC,y}|}{1/2(R_{LC,x} + R_{LC,y})} << 1. \tag{33}$$

Armed with the relation from Eq. 32, we substitute back into Eq. 30 to resolve the energy consumed in the LC tanks during a plasma shot as

$$E_{LC,p} = E_{LC,v}\left(\frac{\int_0^{t_{pulse}} I_{x,p}^2 dt}{\int_0^{t_{pulse}} I_{x,v}^2 dt} + \frac{\int_0^{t_{pulse}} I_{y,p}^2 dt}{\int_0^{t_{pulse}} I_{y,v}^2 dt}\right). \tag{34}$$

Now, we can recast our equation for coupling efficiency as

$$\eta_c = 1 - \frac{V_{BB,v} I_{DC,v}}{V_{BB,p} I_{DC,p}}\left(\frac{\int_0^{t_{pulse}} I_{x,p}^2 dt}{\int_0^{t_{pulse}} I_{x,v}^2 dt} + \frac{\int_0^{t_{pulse}} I_{y,p}^2 dt}{\int_0^{t_{pulse}} I_{y,v}^2 dt}\right). \tag{35}$$

D. Polydispersion Efficiency

The polydispersion efficiency can be calculated from Eq.12 using the measurements from the RPA. The RPA data provides a normalized ion energy distribution function, $f(\varepsilon)$, for each of our averaged time-bins. We can form an expression for the mean ion energy over time as

$$\langle\varepsilon\rangle(t) = \int_0^\infty f(\varepsilon, t)\varepsilon d\varepsilon, \tag{36}$$

where ε is the energy of the ions, and $f(\varepsilon, t)$ is the normalized ion energy distribution from the RPA. Similarly, we can write the root mean squared ion energy over time as

$$\langle\sqrt{\varepsilon}\rangle^2(t) = \left(\int_0^\infty f(\varepsilon, t)\sqrt{\varepsilon} d\varepsilon\right)^2. \tag{37}$$

Since the energy distribution functions are normalized for each time, we weight mean ion energy and root mean squared ion energies by the number of particles collected by the FP as a function of time. This particle flux is written as

$$\Gamma(t) = \pi R^2 \int_0^{\pi/2} \frac{j_{FP}(\theta, t)}{e} \sin(\theta) d\theta, \tag{38}$$

where j_{FP} is the current density measured by the FP, R is the radius of the RPA and FP, and θ is the polar angle the probe arm makes with the thruster. The time-averaged mean energy becomes

$$\overline{N\langle\varepsilon\rangle} = \int_0^{t_{pulse}} \Gamma(t)\langle\varepsilon\rangle(t) dt, \tag{39}$$

and the time-averaged root mean squared energy becomes

$$\overline{N\langle\sqrt{\varepsilon}\rangle^2} = \int_0^{t_{pulse}} \Gamma(t)\langle\sqrt{\varepsilon}\rangle^2(t) dt. \tag{40}$$

We can then use these to substitute into Eq. 12 to calculate the polydispersive efficiency which is now written as

$$\eta_{pd} = \frac{\overline{N\langle\sqrt{\varepsilon}\rangle^2}}{\overline{N\langle\varepsilon\rangle}}. \tag{41}$$

E. Plasma Efficiency

To calculate the plasma efficiency in Eq. 18, we need to determine the thermal and magnetic energy input into the plasma. For this, we assume that the instantaneous maximum energy stored in the thermal and magnetic modes is approximately equal to the energy input into those modes. The instantaneous maximum thermal energy in the plasma can be written as

$$E_{th} = max\left(\frac{5}{2} n(t) k_b T_e(t) V\right), \tag{42}$$

where n is the plasma density, T_e is the electron temperature both from the LP, and V is the thruster volume. Here we assume that the ions are cold and do not contribute significantly to the thermal energy of the plasma and make the generous assumption that density and temperature are spatially uniform. The density, temperature, and instantaneous thermal energy for the three conditions are shown in Fig. 12. The maximum magnetic energy is

$$E_B = max\left(\iiint_V \frac{|\mathbf{B}|^2(t)}{2\mu_0}dV\right), \tag{43}$$

where $\mathbf{B}$ is the induced magnetic field caused by azimuthal plasma currents. We calculate the azimuthal plasma current distribution in the thruster through an analytic Bayesian regression. For this process, we segment the thruster cross-section into discrete area elements elements, as shown in Fig. 9. For every 5 μs time-step throughout the plasma pulse, each discretized area element is assigned a prior distribution for the azimuthal current which passes through it, whose mean is described by

$$j_\theta^0 = \alpha\left(en_n(z)\omega r\right)e^{-\frac{(z-z_{max})^2}{\Delta z^2}}, \tag{44}$$

where α is a scaling factor dependent on the maximum measured magnetic field, ω is the RMF frequency in rad/s, $n_n(z)$ is the neutral density assuming steady state thermal diffusion, z_{max} is the axial location of maximum measured magnetic field, Δz is a assumed distribution width of 10 cm, and r and z are the radial and axial coordinates respectively. The uncertainty of this prior mean is assumed to be 50% of the mean value. These discrete azimuthal current values are treated as the regression parameters. The likelihood is derived by assuming a Gaussian probability distribution for the center line axial magnetic field centered on the values measured from the inductive probes placed along center line. By making the critical assumption that both the prior and likelihood are described by Gaussian distributions, we can leverage the method of conjugate priors, giving an analytic update equation for the current distribution written as

$$j_\theta^{post} = j_\theta^0 + \Sigma^0 A^T(A\Sigma^0 A^T + \Gamma)^{-1}(B_z - Aj_\theta^0) \tag{45a}$$

$$\Sigma^{post} = \Sigma^0 - \Sigma^0 A^T(A\Sigma^0 A^T + \Gamma)^{-1}A\Sigma^0, \tag{45b}$$

where j_θ^{post} and Σ_{post} are the posterior current distribution mean and variance respectively, j_θ^0 and Σ^0 are the prior current distribution mean and variance respectively, A is a matrix to convert the currents to center-line magnetic fields, Γ represents data noise, and B_z is the time series of axial magnetic field measurements. We show in Fig. 9 an example result for this time- and spatially-resolved current map.

Armed with this inferred current distribution, we can calculate the induced magnetic field throughout the thruster domain by the Biot-Sarvart Law; stated here as

$$\mathbf{B}(\mathbf{r}) = \frac{\mu_0}{4\pi}\iiint_V \frac{(j_\theta^{post}\hat{\theta}dV)\times\mathbf{r}'}{|\mathbf{r}'|^3}, \tag{46}$$

where $\mathbf{r}'$ is the vector from the volume dV to the observation point $\mathbf{r}$, and the integral is performed over the thruster volume V. Additionally, for Eq. 45a the axial magnetic fields can be found from the inductive B-dot probes by

$$B_z(t) = \frac{1}{|\beta(\omega)|}\int_0^t V_p\,(\tau)\,d\tau, \tag{47}$$

where $\beta(\omega)$ is a frequency dependent calibration term as described by Polzin et al. [24] and V_p is the voltage output from the probe. The details of this calibration process are presented in Appendix A.

F. Acceleration Efficiency

The last term we need to calculate the acceleration efficiency is the kinetic energy of the plasma slug in the far-field. This kinetic energy can be measured by integrating over the kinetic energy flux using the combined measurements of the FP and RPA. Relying on Eq. 39, we have ready an expression for the kinetic energy in the far-field plume. Re-stated here as

$$E_i = \overline{N\langle\varepsilon\rangle} = \int_0^{t_{pulse}} \Gamma(t)\langle\varepsilon\rangle(t)dt, \tag{48}$$

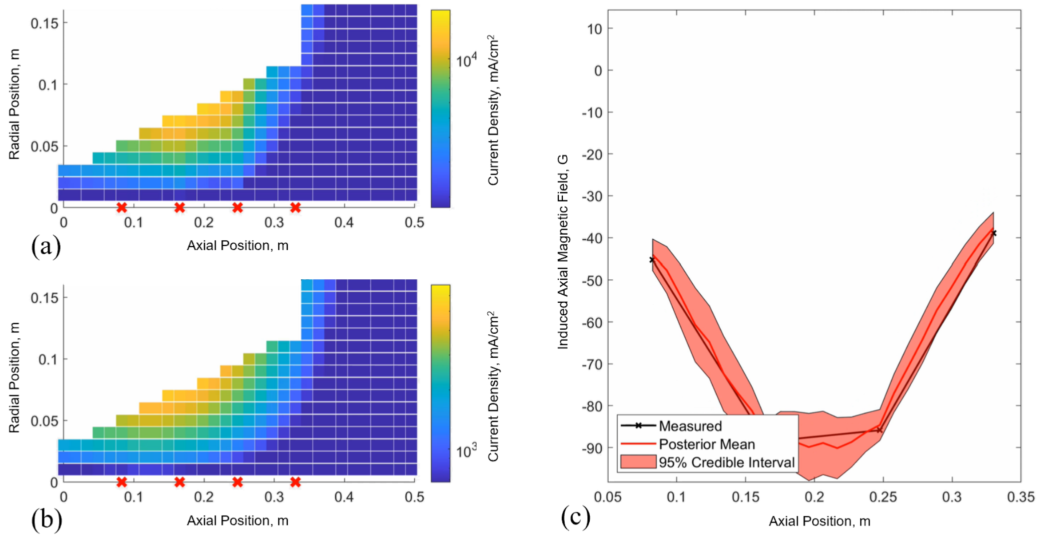

Fig. 9 Example of Bayesian regression technique from 4.0 mg/s at 135 μs showing a) posterior mean current distribution, j_θ^{post}, b) posterior variance, Σ_{post}, and c) measured and calculated axial magnetic fields from B-dot probes and posterior mean current distribution respectively. Red "x's" indicate locations of B-dot probes.

where this physically this represents the time integral of the mean kinetic energy flux of the ions. Armed with E_i and taking E_{th} and E_B from Eqs. 42 and 43 respectively, we can now calculate acceleration efficiency as

$$\eta_a = \frac{E_i}{E_B + E_{th}}. \tag{49}$$

VII. Results

In this section, we present the results of our efficiency characterization for our RMF test article. We begin by restating the global performance results from our previous experimental characterization. Following this, we then show the intermediate results from our near and far-field plasma diagnostic probes and the final calculated efficiency breakdowns for our three flow conditions.

A. Global Performance

We show in Table 2 the measured mass flow rate, input power, impulse, estimated neutral mass, and efficiency for the three flow rates listed in table 1. This data comes from our previous experimental effort to characterize the performance of the PEPL RMFv2 [13] where the thruster was operated at 75 Hz pulse-repetition rate with a pulse length of 200 μs. Several instruments were used to measure the performance characteristics of the thruster: the flow rate was taken as the commanded flow to the to the cathode and neutral diffuser, the input energy per shot was calculated by measuring the power delivered to the PPU while plasma was present, steady thrust was measured via an inverted pendulum thrust stand operating in displacement mode and converted to impulse per shot through the pulse repetition rate, and neutral mass was estimated using the technique described previously. The efficiency is then calculated using Eq. 2.

B. Probe Data

In this subsection, we show the intermediate probe results for the three flow conditions from Table 1. Starting out, in Fig. 10 we show the measured ion charge fluxes as a function of polar angle about the thruster. In these plots, the top axes represents the data in the time domain, and the bottom axes converts this in to the speed domain, where we use the distance of the probe arm to the thruster exit plane—1.5 m—to infer a time-of-flight measurement for ions speed. In these plots, we can see that the ions are traveling between roughly 5 - 8 km/s, however, this does not account for any delay caused by the time for ionization to occur. From the necking of the plasma-loaded RMF waveforms in Fig. 8, we

Table 2 **Per-Pulse Global Performance Results. E_{in} is the input electrical energy, I is the measured impulse, M is the available neutral mass, and η_{TS} is the efficiency measured by the thrust stand.**

Flow rate $[mg/sXe]$	$E_{in}[J]$	$I[\mu Ns]$	$M[kg]$	η_{TS}
2.7	39.1 ± 2.7	64 ± 8	1.8E-08	0.30 ± 0.02%
4.0	42.0 ± 1.2	101 ± 14	2.7E-08	0.45 ± 0.01%
5.4	48.7 ± 0.3	109 ± 4	3.6E-08	0.341 ± 0.002%

can deduce that the ionization time is on the order of 100 μs, as this necking corresponds to increasing plasma density. Knowing this, the actual ion speeds could potentially be up to 10 km/s. There are two other features to note in Fig. 10 as the flow rate is increased. First, the development of a torroidal geometry can be seen through the decreased ion signal present at 90° for the 4.0 and 5.4 mg/s cases. This is an indication of axial magnetic field reversal caused by the azimuthal plasma currents, which is confirmed by our B-dot measurements in Fig. 13. Second, we see the presence of what appears to be two distinct ion populations separated by speed. In the 5.4 mg/s case, in particular, we see a larger slower moving population at ≈ 5 km/s and a smaller but faster group moving at ≈ 7 km/s. This feature may ultimately reflect the fact that the RMF only accelerating a fraction of the ions inductively while the remainder are accelerated thermally.

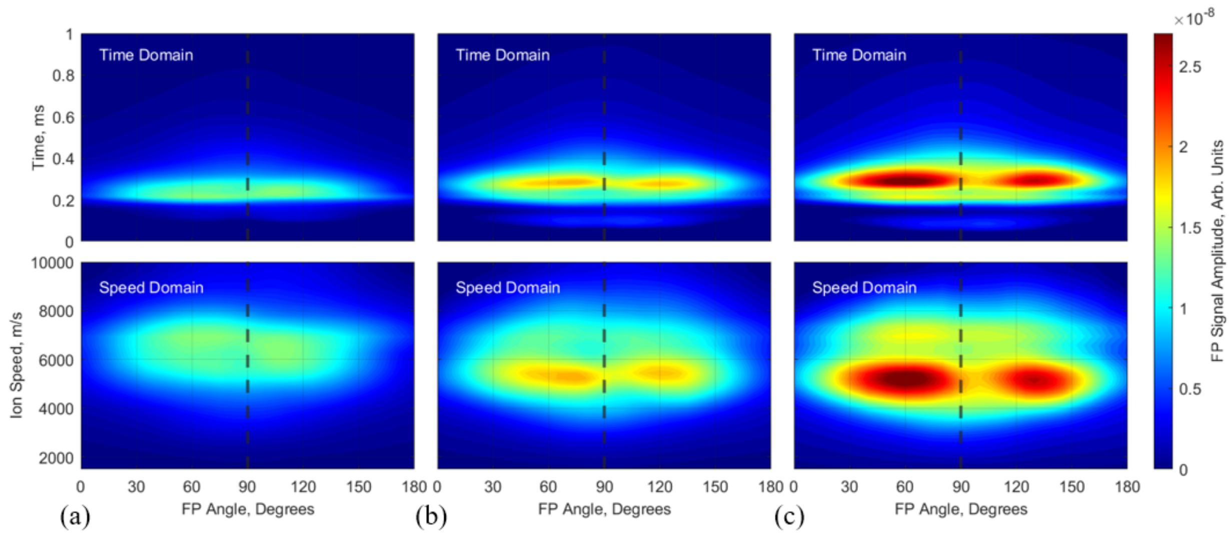

Fig. 10 Faraday probe signal as a function of probe arm angle for three flow rates. a) 2.7 mg/s, b) 4.0 mg/s, and c) 5.4 mg/s. Upper plots show signal as a function of time, lower plots show signal as a function of time-of-flight speed.

Next, in Fig. 11 we show the ion energy probability distribution functions from the RPA measurements as a function of time where the distribution for each time slice is normalized over energy. From the figure, we can see that as the flow rate is increased, we are able to produce higher energy ions with content present between 150 - 200 eV for the 5.4 mg/s case. It is also worth noting here that after approximately 0.4 ms, the ion energies return to their background value from the cathode of around 10-15 eV.

Turning now to the results from our near field probes, we show in Fig. 12 the measured electron temperature and plasma density from the LP, and the calculated stored thermal energy from Eq. 42. As expected, the densities measured in the plasma appear to increase linearly with flow rate with the maximum density measured as $4 \times 10^{18}\text{m}^{-3}$ for the 5.4 mg/s flow condition. Interestingly, we do not measure significant heating of the electrons with temperatures reaching at most 30 eV, and this only occurs towards the end of the measurement roughly after 0.4 ms. One would expect the hottest period to be during or near the RMF discharge. The reason we do not see this is likely due to systematic interference from the RMF on the LP. This effect can be seen in within the first 200 μs in Fig.7.

Continuing in the near-field, we show both the induced axial magnetic fields and the calculated stored magnetic

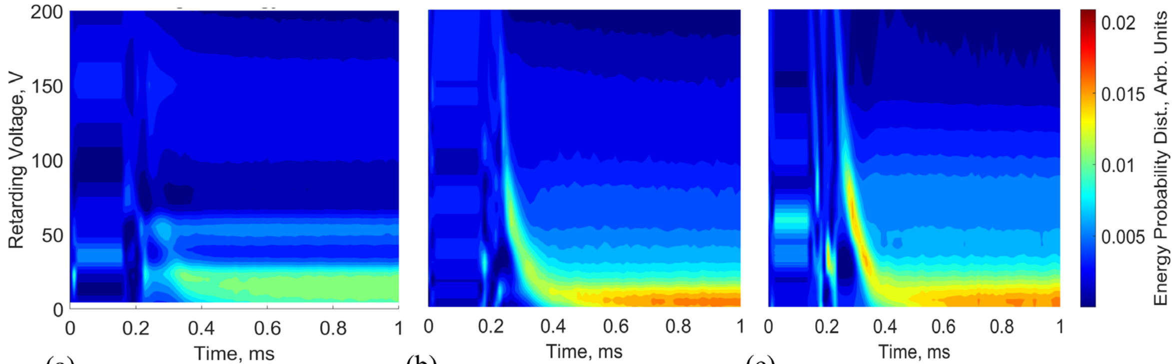

(a) (b) (c)

Fig. 11 Normalized ion energy distribution function derived from RPA measurements as a function of time for the three flow rates: a) 2.7 mg/s, b) 4.0 mg/s, and c) 5.4 mg/s.

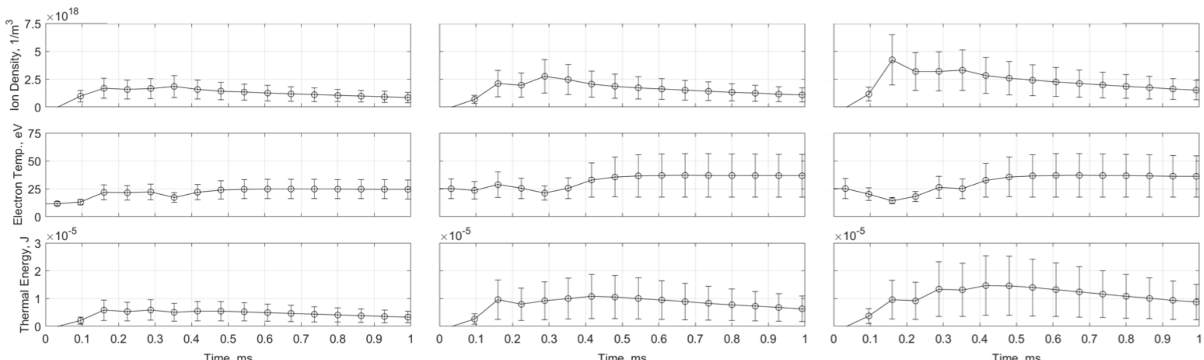

(a) (b) (c)

Fig. 12 Langmuir probe measured quantities over time for three flow rates. a) 2.7 mg/s, b) 4.0 mg/s, and c) 5.4 mg/s. Upper plots show plasma density, middle plots show electron temperature, and lower plots show calculated stored thermal energy from Eq. 42.

energy over time in Fig. 13. The induced magnetic fields shown come from our third B-dot probe located 8.3 cm upstream from the thruster exit plane, and we can see that they reach strengths between 80 and 100 G pointing upstream into the thruster. These field strengths are greater than the axial component of the bias field in this region—less than 50 G—indicating that our plasma currents have reversed the axial field. The stored magnetic energy data directly comes from the evaluation of Eq. 43, and stems from the results of our Bayesian regression for the azimuthal currents described in section VI. Here we can see that for the higher flow rates, more energy is able to be stored in the magnetic field due to an increase in the number of charge carriers. We also see that for the higher flow rates, the onset of energy storage occurs earlier, and this is likely caused by a faster ionization time due to increased collisionality. Lastly, a distinct double hump is seen across conditions. While this could be an artifact of the regression technique,this could also be an explanation for the multiple populations we see from the FP results in Fig. 10. In this case, two inductive pulses would be occurring, where after the initial pulse is evacuated extra neutrals back-fill and are successively ionized and accelerated by excess RMF energy.

C. Efficiencies

We present in Fig. 14 the calculated phenomenological efficiency terms for the three thruster operating conditions. The left hand bar represents the thrust stand measured impulse efficiency, η_{TS}, from Eq. 2. Here we can see that it reaches a maximum at the 4.0 mg/s flow condition, but is overall below 0.5%. The uncertainty in the η_{TS} comes from the standard deviation in the measured thrust for three independent trials. The second bar represents the divergence efficiency, η_d, where the uncertainty is propagated from the standard deviation in the averaged FP currents. Across

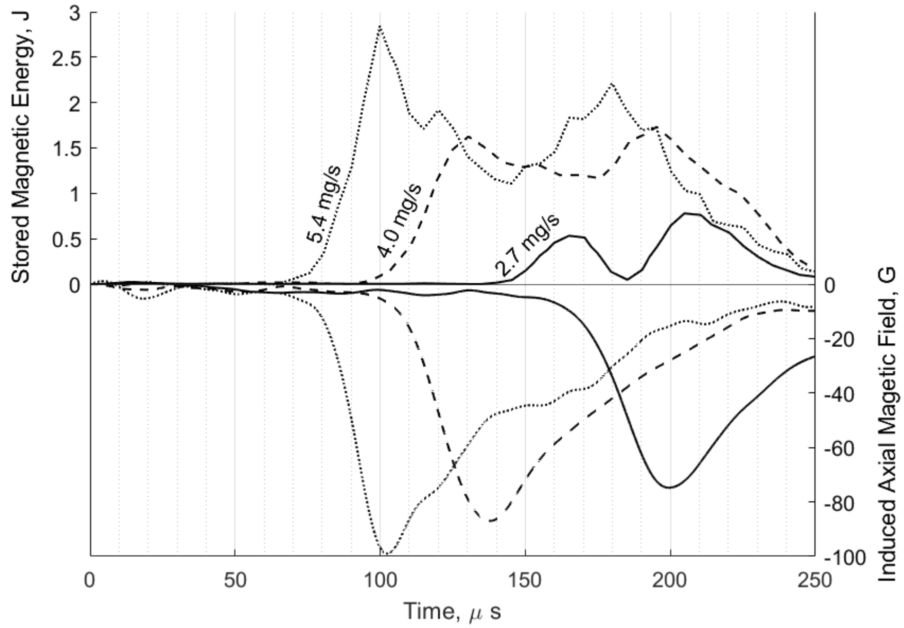

Fig. 13 Upper, stored magnetic energy over time from the presence of azimuthal currents. Lower, induced axial magnetic field on third B-dot probe located 8.3 cm upstream from exit plane.

conditions, this mode constitutes approximately a 60% energy loss with slightly larger beam divergence as density increases leading to a lower efficiency at higher flow rates. This high divergence is likely caused by the rapidly diverging bias magnetic field near the exit plane of the thruster. The third bar is the mass utilization efficiency, η_m, where the uncertainty again comes from the FP measurement. We find the mass utilization is near unity for all cases, with the 2.7 mg/s case the lowest at 92%. This indicates that the RMF is sufficiently capable of ionizing nearly all the neutral particles available to it. The fourth bar is the polydispersion efficiency, η_{pd}, and the uncertainty comes from the propagated standard deviation of the RPA measurements. Our measured polydispersion efficiencies are sufficiently low for the RMF plume not to be considered mono-energetic. Here, η_{pd} is around 85% for all the flow conditions. This is due solely to the width of RPA energy distributions and is an indication that the ions in the plume are being accelerated to a range of speeds. The next bar is the coupling efficiency, η_c, where—similar to η_{TS}—the uncertainty comes from the standard deviation of three independent measurements. We note here that coupling η_c is around 35% meaning 65% of the energy delivered to the RMF PPU does not couple into the plasma. Also, we see that the coupling efficiency increases with flow rate because at higher plasma densities there are more electrons for the RMF to couple energy into. The sixth bar from the left is the plasma efficiency, η_p, and the uncertainty stems from both the error in the energy coupled into the plasma and the maximum energies stored in the thermal and magnetic modes. The uncertainty of the thermal energy measurement comes from the typical uncertainties of a LP, and we assume the uncertainty of the magnetic energy via the Bayesian regression process is 20%. This efficiency mode is our largest detriment to performance reaching at most 14 % for the high flow condition. Physically, this means the majority of the energy absorbed by the plasma from the RMF is unrecoverable. The second to last bar in Fig. 14 is the acceleration efficiency, η_a, and the uncertainty comes from the thermal and magnetic energy measurements as described above, and the combined standard deviations of the shot-averaged RPA and FP measurements. Since η_a is near unity for our conditions, we can intuit that the energy in the azimuthal electron current and/or stored thermally is effectively converted to downstream directed kinetic energy. Although, we do see that this conversion becomes less efficient as flow rate increases. The right most bar is the probe-measured efficiency, η_{probe}, and is the product of the six phenomenological efficiency terms in Eq. 20. We can see that η_{probe} overpredicts η_{TS} by a factor of roughly 3-4 but is in the same range reaching at most 1.5%.

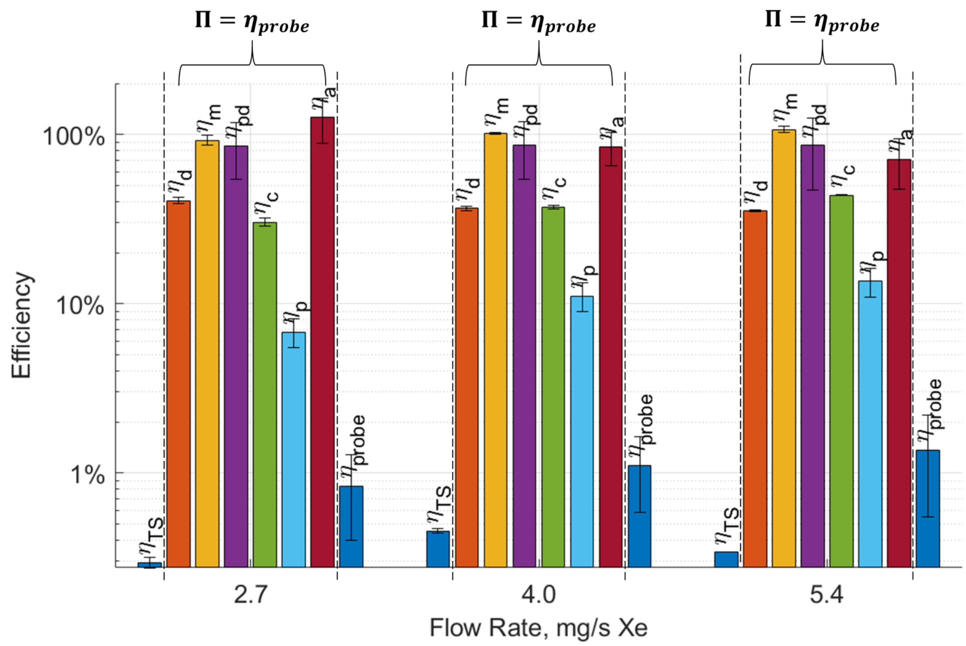

Fig. 14 Efficiency break down versus flow rate. The left most bar corresponds to thrust stand measured impulse efficiency, and the right most bar corresponds to the product of the six probe-measured efficiency terms.

VIII. Discussion

A. Difference Between Performance Measurements and Probe Measurements

As is evident from Fig. 14, our calculated total probe measured efficiencies over predict the thrust stand measured efficiencies by a factor of 3-5. This is likely caused by a few different effects. First, A major caveat to our thrust stand efficiencies is the assumption we made about steady thermal diffusion to determine the available neutral mass. An improved technique would be to spatially measure the steady-state neutral pressure to determine the prior neutral density before RMF spin-up and this may alter the total impulse efficiencies we calculate. Second, we saw throughout this experiment that the presence of the RMF imposed systematic error on our electrostatic probes. As an example, this can be seen in the averaged waveform for FP current in Fig. 7. In this trace, the 400 kHz RMF noise is close to averaged out; however, there exists negative current collected at the pulse onset which is non-physical for the operation of a negatively biased FP. We do not yet understand the root cause of this effect; however, mitigation strategies will be explored in future experiments. The final—and likely dominant—cause for our over prediction is the calculation of the average downstream kinetic energy for η_a. The acceleration efficiency has the second highest uncertainty of our phenomenological efficiencies which is on the order of ±20%. This large uncertainty stems from the RPA measurement, which in-itself has uncertainties on the order of 100%. Additionally, we only performed RPA measurements of the ion energies along the thruster axis and assume this remains constant throughout the plume. However, this may not be appropriate considering the non-monotonic behaviour of ion flux seen by the FP, as the peak signal occurs off axis as in Fig 10. Furthermore, since η_a trends down with increasing flow rate, an improved measurement may reveal the local maximum seen in η_{TS}.

B. Mass utilization

The mass utilization efficiencies measured in this experiment are not a dominant loss factor to overall thruster performance. This is a notable contrast to previous computational work by Brackbill et al. [14], where it was indicated that mass utilization could contribute a significant efficiency loss for RMF thrusters due to the interaction of a propagating ionization front with dense downstream neutrals. However, a caveat to this result is our assumption of the available neutral mass within a pulse. It may be the case that the ejected plasma is able further ionize neutral gas in the far-field thus making our neutral mass estimate artificially low. A true test of mass utilization efficiency could be performed by operating the thruster at a pulse repetition rate commensurate with the characteristic neutral re-fill rate such that no propellant can be considered "wasted" during the RMF dead-time.

C. Acceleration Efficiency

The acceleration efficiencies we calculated are all near unity, meaning that the conversion process from thermal and magnetic energy to directed kinetic energy is very efficient in the RMF thruster. However, as we noted previously, this term comes with a large uncertainty, and the calculation could be improved by taking spatially resolved RPA measurements. Additionally, we knowingly overestimate the value of η_a by assuming the instantaneous stored thermal and magnetic energy in the plasma is approximately the energy input into those modes. This is explained by looking at the input energy for a given mode—either thermal or magnetic— which can be stated as

$$E_{\text{mode,in}} = \int_0^{t_{pulse}} P_{\text{mode,in}}(\tau) d\tau, \tag{50}$$

where $P_{\text{mode,in}}$ is the input power into that mode. However, our measurements only quantify the instantaneous energy that exists in a given mode; this is written as

$$E_{\text{mode}}(t) = \int_0^{t} P_{\text{mode,in}}(\tau) - P_{\text{mode,out}}(\tau) d\tau, \tag{51}$$

where $P_{\text{mode,out}}$ now represents the power drained from this mode. Given the above equations, we can see that $E_{\text{mode}}(t) \leq E_{\text{mode,in}}$ for all time t, but we assume that $max(E_{\text{mode}}(t)) \approx E_{\text{mode,in}}$. Because of this assumption, the calculated acceleration efficiency is an upper bound for the true acceleration efficiency.

D. Polydispersion Efficiency

Our measured polydispersion efficiencies are all roughly 85%. As mentioned in section IV, this does not represent an energy loss per se; but, it is an indication that some of our ions are not accelerated as effectively as they could be. The main way to improve this term would be to boost the inductive drive of the RMF thruster by increasing antenna currents. This would ensure that the RMF is fully penetrating through the plasma column and is able to couple to all the available electrons. However, it maybe the case that our result for polydispersion efficiency stems from the fact that the Lorentz force will be inherently weaker towards the center of the thruster since the electron current will be linearly proportional to its radial distance. While this could be mitigated by implementing an annular thruster geometry, this may be an unavoidable characteristic of RMF thrusters.

E. Coupling Efficiency

Our calculated coupling efficiencies range between 30 - 44% and increase with flow rate. Physically, this means that the plasma is only able to absorb a fraction of the energy introduced to the LC tanks. For this study, we did not attempt to optimize for high coupling efficiency. However, our coupling efficiency could likely be improved by shortening the pulse length. The rebounding antenna current shown in Fig. 8 after roughly 125 μs is an indication that the plasma is losing its ability to accept energy from the RMF and additional input energy at this time will ultimately dissipate in the PPU circuitry. Shortening the RMF pulse length to correspond with the antenna current minimum could therefore prove beneficial for improving coupling efficiency.

F. Divergence Efficiency

The divergence efficiency for the RMF thruster is low because the plume is not very collimated. This can be clearly seen in Fig. 3(b) through the steep angle the plasma fluorescence makes with the thruster exit plane. This large divergence is likely the result of the sharply diverging magnetic bias field in this region [13]. By carefully shaping the magnetic field near the thruster exit, it could be possible to better collimate the plasma to improve divergence efficiency.

G. Plasma Efficiency

From Fig. 14, plasma efficiency η_p is evidently the dominant loss mechanism for the three operation conditions investigated as it constitutes a roughly 90% loss from the energy coupled to the plasma. As shown in Eq. 18 plasma efficiency is calculated by taking the ratio of the peak thermal and magnetic energy in the plasma to the energy coupled into the plasma from the RMF. However, it remains an open question where the majority of the energy is lost. Restated from Eq. 14, we can write the energy coupled to the plasma as a sum of several energy loss and storage terms

$$E_p = E_{th} + E_B + E_{iz} + E_{rad} + E_{wall} + ..., \tag{52}$$

where E_{th} is the thermal energy of the plasma, E_B is the magnetic energy of the azimuthal currents, E_{iz} is the energy cost of ionization, E_{rad} is the energy lost due to radiated power from excitation collisions, and E_{wall} is the energy lost through diffusion to the thruster walls. We state in Eq. 42 and Eq. 43 the calculation for thermal and magnetic energy respectively, and we can calculate the three loss terms E_{iz}, E_{rad}, and E_{wall} by the following. First, the energy for ionization comes from

$$E_{iz} = \frac{M_i}{m_i} * \epsilon_{iz}, \tag{53}$$

where ϵ_{iz} is the first ionization energy for Xe, $\epsilon_{iz} = 12.13\, eV$ [25], and M_i is the total ion mass from Eq. 27. We again assume here that all the ions are singly charged and they each require an energy input of ϵ_{iz}. The plasma radiated energy is calculated as

$$E_{rad} = \int_0^{t_{\text{pulse}}} n^2 \langle \sigma_{ex} v_e \rangle \epsilon_{ex} V dt, \tag{54}$$

where $\langle \sigma_{ex} v_e \rangle$ is the excitation reaction rate from [26], and $\epsilon_{ex} = 8.3\, eV$ is the energy per excitation collision [27]. The radiated energy scales as the square of plasma density, as we only consider electron-ion excitation collisions and neglect the contributions from excited neutrals. Lastly, the energy lost to the wall is

$$E_{wall} = 0.5 \int_0^{t_{\text{pulse}}} A_{wall} n \sqrt{\frac{k_b T_e}{m_i}} (2k_b T_e + e\phi) dt, \tag{55}$$

where A_{wall} is the inside area of the thruster, m_i is the ion mass, and ϕ is the plasma potential. Physically, this equation is the time-integrated power that the electrons carry to the floating thruster wall, where $\sqrt{k_b T_e m_i}$ is the Bohm speed, and the parenthetical term is the energy lost per electron.

We have evaluated the five identified contributions to plasma energy listed in Eq. 52 and present them Table 3.

Table 3 Constituent Components of Plasma Energy.

Flow [mg/s]	$E_{th} + E_B$ [J]	E_{iz} [J]	E_{rad} [J]	E_{wall} [J]	Sum [J]	E_p [J]
2.7	0.8 ± 0.2	0.15 ± 0.03	0.8 ± 0.2	3.0 ± 0.3	4.7 ± 0.4	11.8 ± 0.5
4.0	1.7 ± 0.3	0.23 ± 0.05	1.6 ± 0.4	7.4 ± 1.0	11.0 ± 1.1	15.6 ± 0.2
5.4	2.9 ± 0.6	0.31 ± 0.06	3.2 ± 0.7	8.5 ± 1.1	14.9 ± 1.5	21.3 ± 0.1

From Table 3, we can see that energy flux to the walls is the largest contributor to losses in the plasma by a considerable margin. It is worth noting that the calculated terms in Table 3 are the result of a simplified 0D analysis of the plasma, primarily because we only resolved plasma parameters from one fixed Langmuir probe position. For example, for the wall loss calculation we assume the electrons can freely flow to the wall without magnetic confinement, and we assume properties are spatially uniform. It is interesting that our low-fidelity analysis reveals wall losses as a dominant factor, as our RMF test article does not incorporate the axial flux conservers present in other RMF thrusters [12, 28]. We forwent the flux conservers for the sake of improving the acceleration of the plasma; however, this eliminated the increased magnetic confinement the flux conservers typically provide. A caveat to make here is that in our calculation of wall losses we did not take into account the impact the bias or self magnetic fields will have in reducing the electron flux to the walls and assume electrons can travel freely along the RMF field lines. However, at 2 kA antenna current the RMF field strength is on the same order as the bias field and will drive the initially parallel field lines into the wall. Looking at the final two columns of Table 3, we can also see that the sum of the identified terms from Eq. 52 does not completely explain the energy absorbed by the plasma, E_p. There is a consistent delta of roughly 5 J across flow rates that could be caused by a systematic error in our estimates. This error would likely be the result of our assumption that density is uniform throughout the thruster, and a spatially resolved density measurement could lead to higher estimates for E_{rad}, and $E_w all$ that may fully explain the losses. However, an unidentified loss term may also be the explanation for the missing energy. Either excitation collisions with the neutrals, particularly during the onset of plasma formation when neutral densities are large, or wave-driven instabilities leading to anomalous resistivity may both be important to consider for a satisfactory explanation of energy loss within the plasma.

H. Implications for Thruster Design

The efficiency breakdown results in Fig. 14 reveal that the primary loss mechanisms in our RMF test article are the divergence, coupling, and plasma efficiencies. The first two of these, divergence and coupling, represent areas where technological advancement could improve thruster performance. The coupling of energy from the RMF to the plasma could be improved by—as mentioned above—matching the RMF pulse time to the formation and ejection time of the plasma. Additionally, coupling could be increased through the addition of more RMF antenna phases to increase uniformity of the RMF field [29]. The divergence efficiency could also in theory be increased by an optimization of the magnetic bias field near the thruster exit to promote axial ejection. For plasma efficiency however, we do not yet have a definitive explanation of the physical mechanism behind the losses within the plasma. It therefore remains to be seen whether this low plasma efficiency will impose a theoretical limit on RMF thruster performance. If the losses are primarily caused by electron flux to the walls, there may be improvements found though additional magnetic confinement, shielding, or the reintroduction of flux conservers. However, the losses may indeed be the result of unidentified physical processes such as increased wave-driven resistivity in the plasma caused by RMF turbulence, which we have not yet characterized. In this case, if it is difficult to eliminate or reduce this energy loss, the plasma efficiency could pose a fundamental limitation to RMF thruster performance.

IX. Conclusion

In this work, we have measured the relative contributions of a phenomenological efficiency model for RMF thrusters. To this end, we derived a efficiency breakdown for RMF thrusters and defined physically significant terms, and we performed a comprehensive diagnostic probe study to measure the plasma properties in the near and far-field. We found that plasma efficiency was the most significant detriment to total impulse efficiency and represents that the majority—up to 93%—of the energy coupled to the plasma is unrecoverable as directed kinetic energy downstream. A preliminary 0D analysis of the energy flow within the plasma indicates that most of the energy coupled to the plasma is lost to the thruster walls. This is an insightful result, as the test article used in this experiment was designed without the flux conservers conventionally used to magnetically confine the plasma. Now that the primary loss mechanism had been identified, we can work to take better measurements of the underlying physical properties with the ultimate goal of improving RMF thruster performance.

X. Acknowledgements

We would like to acknowledge the technical support of Eric Viges from the University of Michigan in regards to the fabrication of the RMF power lines. Furthermore, we would like to thank Dr. James Prager, Dr. Ken Miller, and Kyle McEleney from Eagle Harbor Technologies for their development of the RMF power processing unit and technical support. Funding for this work was supplied under an Air Force SBIR grant, NSTGRO Fellowship grant Number 80NSSC20K1168, NSTRF Fellowship grant number 80NSSC18K1190, and the AFOSR Space Propulsion and Power portfolio.

References

[1] Berg, S. P., and Rovey, J. L., “Assessment of High-Power Electric Multi-Mode Spacecraft Propulsion Concepts,” *IEPC*, 2013, pp. 1–11.

[2] Rovey, J. L., Lyne, C. T., Mundahl, A. J., Rasmont, N., Glascock, M. S., Wainwright, M. J., and Berg, S. P., “Review of multimode space propulsion,” *Progress in Aerospace Sciences*, Vol. 118, 2020, p. 100627. https://doi.org/10.1016/j.paerosci.2020.100627, URL https://doi.org/10.1016/j.paerosci.2020.100627.

[3] Polzin, K. A., Martin, A. K., Little, J., Promislow, C., Jorns, B. A., and Woods, J. M., “State-of-the-art and advancement paths for inductive pulsed plasma thrusters,” *Aerospace*, Vol. 7, No. 8, 2020, pp. 1–67. https://doi.org/10.3390/AEROSPACE7080105, URL https://www.mdpi.com/2226-4310/7/8/105.

[4] Mikellides, P. G., and Villarreal, J. K., "High energy pulsed inductive thruster modeling operating with ammonia propellant," *Journal of Applied Physics*, Vol. 102, No. 10, 2007, pp. 1–12. https://doi.org/10.1063/1.2809436.

[5] Polzin, K. A., "Comprehensive review of planar pulsed inductive plasma thruster research and technology," *Journal of Propulsion and Power*, Vol. 27, No. 3, 2011, pp. 513–531. https://doi.org/10.2514/1.B34188, URL http://arc.aiaa.org/doi/10.2514/1.B34188.

[6] Mikellides, P. G., "Pulsed Inductive Thruster (PIT): Modeling and Validation Using the MACH2 Code," Tech. Rep. 480, NASA, 2003. URL http://hdl.handle.net/2060/20040027584.

[7] Slough, J. T., Kirtley, D. E., and Weber, T. E., "Pulsed Plasmoid Propulsion: The ELF Thruster," *31 th International Electric Propulsion Conference*, 2009, pp. 1–24. URL https://s3-us-west-2.amazonaws.com/pnwmsnw/ELF_IEPC-2009-265.pdf.

[8] Weber, T., "The Electrodeless Lorentz Force Thruster Experiment," Ph.D. thesis, University of Washington, 2010. URL https://digital.lib.washington.edu/researchworks/handle/1773/20069.

[9] Kirtley, D. E., Slough, J. T., Pfaff, M., and Pihl, C., "Steady Operation of an Electromagnetic Plasmoid Thruster," Tech. rep., MSNW, 2011.

[10] Waldock, J., Kirtley, D. E., and Slough, J. T., "Electromagnetic Optimization of FRC-Based Pulsed Plasma Thrusters," *33rd International Electric Propulsion Conference*, 2013, pp. 1–14.

[11] Furukawa, T., Shimura, K., Kuwahara, D., and Shinohara, S., "Verification of azimuthal current generation employing a rotating magnetic field plasma acceleration method in an open magnetic field configuration," *Physics of Plasmas*, Vol. 26, No. 3, 2019. https://doi.org/10.1063/1.5064392, URL http://dx.doi.org/10.1063/1.5064392.

[12] Furukawa, T., Shinohara, S., and Kuwahara, D., "Electrodeless plasma propulsion with electromagnetic acceleration effect by using rotating magnetic field current drive method," *AIAA Propulsion and Energy 2020 Forum*, 2020, pp. 1–11. https://doi.org/10.2514/6.2020-3630.

[13] Sercel, C. L., Gill, T., Woods, J. M., and Jorns, B., "Performance Measurements of a 5 kW-Class Rotating Magnetic Field Thruster," *AIAA Propulsion and Energy 2021 Forum*, American Institute of Aeronautics and Astronautics, 2021, pp. 1–26. https://doi.org/10.2514/6.2021-3384, URL https://arc.aiaa.org/doi/10.2514/6.2021-3384.

[14] Brackbill, J., Cambier, J. L., Gimelshein, N. E., and Gimelshein, S. F., "Numerical analysis of neutral entrainment effect on field-reversed configuration thruster efficiency," *Journal of Propulsion and Power*, Vol. 30, No. 6, 2014, pp. 1450–1458. https://doi.org/10.2514/1.B35260.

[15] Woods, J. M., Sercel, C. L., Gill, T. M., and Jorns, B. A., "Performance measurements of a rotating magnetic field thruster," *AIAA Propulsion and Energy 2020 Forum*, Vol. 3633, 2020, pp. 1–18. https://doi.org/10.2514/6.2020-3633.

[16] Miller, K. E., Prager, J., Henson, A., McEleney, K., Woods, J., Sercel, C., Gill, T., Viges, E., and Jorns, B., "Continuously-Operating Repetitively-Pulsed RMF-FRC Thruster and Power System," *2021 IEEE International Conference on Plasma Science (ICOPS)*, 2021, pp. 1–1.

[17] Liang, R., and Gallimore, A. D., "Far-Field Plume Measurements of a Nested-Channel Hall-Effect Thruster," *49th AIAA Aerospace Sciences Meeting including the New Horizons Forum and Aerospace Exposition*, 2011, pp. 1–22. https://doi.org/10.2514/6.2011-1016.

[18] Hofer, R. R., and Gallimore, A. D., "High-specific impulse Hall thrusters, part 2: Efficiency analysis," *Journal of Propulsion and Power*, 2006. https://doi.org/10.2514/1.15954.

[19] Linnell, J. A., and Gallimore, A. D., "Efficiency analysis of a hall thruster operating with krypton and xenon," *Journal of Propulsion and Power*, 2006. https://doi.org/10.2514/1.19613.

[20] Sercel, C. L., Woods, J. M., Gill, T. M., and Jorns, B. A., "Impact of flux conservers on performance of inductively driven pulsed plasmoid thrusters," *AIAA Propulsion and Energy 2020 Forum*, 2020, pp. 1–17. https://doi.org/10.2514/6.2020-3632.

[21] Viges, E. A., Jorns, B. A., Gallimore, A. D., and Sheehan, J., "University of Michigan's Upgraded Large Vacuum Test Facility," *36th International Electric Propulsion Conference*, 2019, pp. 1–18.

[22] Polk, J. E., Pancotti, A., Haag, T., King, S., Walker, M. L. R., Blakely, J., and Ziemer, J., "Recommended practice for thrust measurement in electric propulsion testing," *Journal of Propulsion and Power*, Vol. 33, No. 3, 2017, pp. 539–555. https://doi.org/10.2514/1.B35564.

[23] Brown, D. L., Walker, M. L. R., Szabo, J., Huang, W., and Foster, J. E., "Recommended practice for use of faraday probes in electric propulsion testing," *Journal of Propulsion and Power*, Vol. 33, No. 3, 2017, pp. 582–613. https://doi.org/10.2514/1.B35696, URL https://doi.org/10.2514/1.B35696.

[24] Polzin, K. A., Hill, C. S., Turchi, P. J., Burton, R. L., Messer, S., Lovberg, R. H., and Hallock, A. K., "Recommended practice for use of inductive magnetic field probes in electric propulsion testing," *Journal of Propulsion and Power*, Vol. 33, No. 3, 2017, pp. 659–667. https://doi.org/10.2514/1.B35406.

[25] Brandi, F., Velchev, I., Hogervorst, W., and Ubachs, W., "Vacuum-ultraviolet spectroscopy of Xe: Hyperfine splittings, isotope shifts, and isotope-dependent ionization energies," *Physical Review A*, Vol. 64, No. 3, 2001, p. 032505.

[26] Goebel, D. M., and Katz, I., *Fundamentals of Electric Propulsion: Ion and Hall Thrusters*, Jet Propulsion Laboratory, California Institute of Technology, 2008. https://doi.org/10.1002/9780470436448.

[27] Hayashi, M., "Determination of electron-xenon total excitation cross-sections, from threshold to 100 eV, from experimental values of Townsend's α," *Journal of Physics D: Applied Physics*, Vol. 16, No. 4, 1983, p. 581.

[28] Weber, T. E., Slough, J. T., and Kirtley, D. E., "The electrodeless Lorentz force (ELF) thruster experimental facility," *Review of Scientific Instruments*, Vol. 83, No. 11, 2012, pp. 83,113509. https://doi.org/10.1063/1.4759000.

[29] Hugrass, W. N., "Influence of the Spatial Harmonics on the Rotating Magnetic Field Current Drive." *Australian Journal of Physics*, Vol. 39, No. 4, 1986, pp. 513–527. https://doi.org/10.1071/PH860513.

A. B-dot Calibration

The B-dot probes used in this experiment are calibrated as a function of frequency using a known source. Each B-dot probe was placed inside a Helmholtz pair while situated inside the vacuum chamber near the thruster in a measurement-like configuration. The Helmholtz pair was then driven by a sine wave from a signal generator that was swept from 0-500 kHz. The measured voltage output of the probe was combined with the known time derivative of magnetic field generated by the Helmholtz pair to a generate a frequency dependent transfer function for each probe. An example transfer function in shown in Fig. 15.

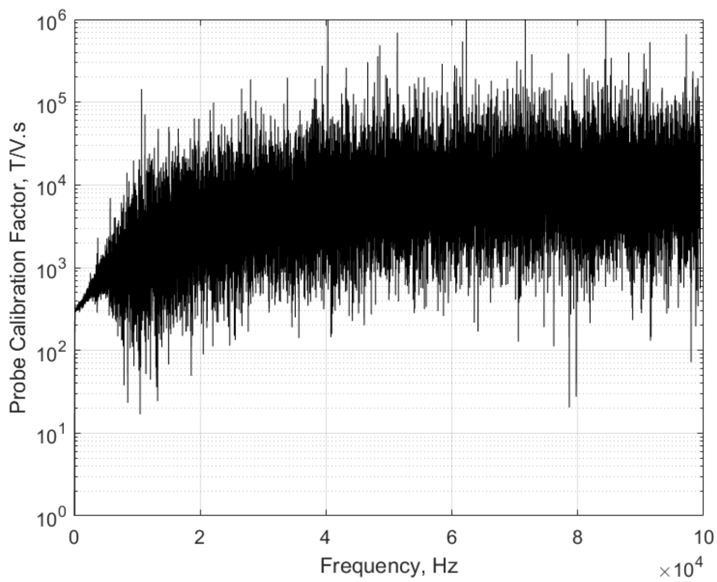

Fig. 15 Example transfer function for B-dot probes as a function of frequency, $\beta(\omega)$.